HIGH-VELOCITY PRESSURE LOSS IN SANDSTONE FRACTURES: MODELING AND EXPERIMENTS

[1]E. Skjetne, [2]T. Kløv and [2]J. S. Gudmundsson

[1]Statoil, N-4035 Stavanger, Norway.
[2]Department of Petroleum Engineering and Applied Geophysics, Norwegian University of Science and Technology, N-7034 Trondheim Norway.

ABSTRACT

High-velocity pressure loss in Berea sandstone fractures was measured and analyzed with a new model. The Berea fracture geometry was measured, and modeled as two identical impermeable self-affine surfaces spaced by a fixed width normal to the average fracture plane. High-velocity pressure loss in a self-affine rough channel was assumed to be proportional to the force of centripetal acceleration as the flow impinges on and bends around obstructions. The modeled pressure loss is square in velocity, and a power law in fracture width, and the power is given by the roughness exponent. We argue that the model may be valid for three-dimensional self-affine rough fractures. Gas flow experiments on fractures with varying widths were performed. High-velocity pressure loss was described by a sum of a linear and a square term in velocity with the Forchheimer equation. The dominating square term was a power law in fracture width, and the power was close to the power predicted by the model. For some of the greater fracture widths, the linear term was negative. For low velocities the Forchheimer equation was not valid. This is in accordance with theory, which states that the Darcy and Forchheimer flow regimes are separated by a weak inertial flow regime.

INTRODUCTION

In this article we study high-velocity pressure loss in rough fractures with a constant vertical width normal to the average fracture plane. It is studied by analytical modeling and flow experiments in Berea cores with an induced fracture. Applications of high-velocity pressure loss in open fractures include: 1) near well hydraulic fractures which are devoid of proppants due to cleanup (*pinched-out* fractures), 2) thermal fractures in water injectors which are kept open by the injection pressure, and 3) natural fractures.

Traditionally, fracture surfaces were modeled as two parallel plates. Experiments show that induced fracture surfaces $z(x,y)$ in brittle materials are statistically self-affine (fractal) surfaces. Statistically they do not change when they are resized according to $l^{-z} z(lx, ly)$, where $l > 0$ is a scale parameter, and $z \in [0, 1]$ is the roughness exponent (also called Hurst exponent). Self-affine fracture roughness profiles are similar to cracks seen on concrete walls. A variety of brittle materials have a fracture surface roughness exponent of about $z = 0.8$. Sandstones may have a somewhat smaller roughness exponent, since exponents were reported in the range of 0.5 - 0.8 (Schmittbuhl *et al.*1996, Boffa *et al.* 1998, Skjetne *et al.* 1998).

Now, steady laminar flow in porous media and fractures is fully described by the mass and momentum conservation (Navier-Stokes) equations plus the geometry (boundary conditions). The ratio between inertial and viscous fluid forces is estimated by a Reynolds number *Re*

$$Re = \frac{\rho l v}{\mu}, \qquad (1)$$

where ρ is the fluid density, μ is the fluid viscosity, l is a characteristic microscopic length scale, and v is a characteristic microscopic velocity. For a high enough Reynolds number the non-linear inertial terms (spatial variations in flow direction and speed) in the Navier-Stokes equations become significant and affect the velocity and pressure fields so that the pressure loss increases more than predicted by Darcy's law. Since a fracture may be viewed as a long pore, we will discuss high-velocity flow in fractures in the context of flow in porous media.

High-velocity flow in porous media is described by the Forchheimer equation (Forchheimer 1901)

$$-\frac{dp}{dx} = \frac{m}{k}V + b\,r\,V^2, \tag{2}$$

where p is the pressure, x is the distance in the flow direction, k is the permeability, V is the seepage velocity (total volume averaged velocity), and b is the inertial resistance which is also called b-factor. The inertial resistance of porous media is typically correlated by a power law (Firoozabadi and Katz 1979)

$$b = \frac{b}{k^a f^c}, \tag{3}$$

where a, b and c are constants, and f is the porosity. Often correlations are made without the porosity dependency, that is with $c = 0$. Since the unit of k is [length^2] and the unit of b is [1/length], media which are scaled copies of each other have $a = 0.5$. Correlations for natural porous media have typically $a \approx 1$. This indicates that a reduction of permeability, for the natural porous media contributing to the correlations, is not only a result of decrease in pore size, but also an increase in complexity of the pore geometry.

Studies show that the Darcy and Forchheimer flow regimes are separated by a weak inertia flow regime, which is described by the weak inertia equation (Barrére 1990, Mei and Auriault 1991, Wodie and Levy 1991, Firdadouss and Guermond 1995, Skjetne and Auriault 1999a)

$$-\frac{dp}{dx} = \frac{m}{k}V + \frac{g\,r^2}{m}V^3, \tag{4}$$

where g is a dimensionless constant. Since the Forchheimer equation is not an extension of Darcy's law, the Forchheimer permeability is a distinct permeability, and we rewrite the Forchheimer equation as

$$-\frac{dp}{dx} = \frac{m}{k_{fh}}V + b\,r\,V^2, \tag{5}$$

where k_{fh} is the Forchheimer permeability. Turbulent flow is also distinct (Skjetne and Auriault 1999b).

Pressure loss for steady incompressible flow in periodic porous media was interpreted alternatively as *energy* and *force* balance (Skjetne and Auriault 1999b). The energy view states that the pressure loss is loss of potential energy (or pressure) by viscous energy dissipation; mechanical energy turns into heat. The force view states that the pressure gradient is due to forces acting on the pore walls by the fluid in terms of a viscous drag, and a pressure (or form) drag from the part of the pressure which varies spatially around the macroscopic pressure decrease in the pore space. The inertial forces scale as the Forchheimer term. Centripetal acceleration was discussed by Noman and Archer (1987). The difference between a Bernoulli stagnation pressure and the pressure in a wake may form a pressure drag (Du Plessis 1994). The viscous effects, which in the energy view must accompany any pressure drag, are still far from well understood.

Let us turn to flow in fractures. Low velocity flow between two parallel plates results in a permeability of $w^2/12$, where w is the fracture width. Low velocity flow in rough fractures depends on the size of the roughness (Brown 1987, Gutfraind and Hansen 1995, Zimmermann and Bodvarsson 1996, Bertuzzi *et al.* 1998). Additional effects were found for multiphase flow (Mahoney and Doggett 1997, Fourar and Lenormand 1998). High-velocity flow in natural fractures resulted in a strong Forchheimer effect (Schrauf and Evans 1986, Jones *et al.* 1988). Data for flow in a periodic fracture (Rasoloarijaona and Auriault 1994) were reexamined and the weak inertia and Forchheimer flow regimes were distinguished (Skjetne and Auriault 1999a). A numerical solution of the Navier-Stokes equations for laminar flow in a self-affine rough channel with $z = 0.8$ showed a clear distinction between Darcy, weak inertia and Forchheimer flow regimes (Skjetne *et al.* 1999). The inertial resistance was a result of high-velocity flow tubes that impinged on obstructing walls and with recirculation zones on the lee side of obstructions.

For high enough velocities, a pressure drag will dominate over a viscous drag, so we focus on the pressure drag. When a flow tube impinges on an obstruction, such as shown in Figure 1, a local centripetal acceleration pressure increase is generated on the front of the obstruction. When the flow tube bends around the peak of the obstruction, there is a local pressure decrease at the lee (recirculation) side. Such centripetal acceleration effects will lead to a systematically higher pressure on the frontal side than on the lee side of

obstructions, and thereby lead to a pressure drag. The pressure drag is a net pressure force inserted by the fluid on the fracture walls in the average flow direction.

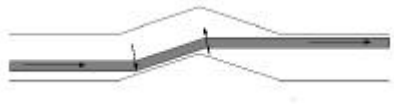

Figure 1. Schematic showing how a flow tube (arrows parallel indicate flow direction) bends around an obstruction. Arrows normal to the flow tube points in the direction of increasing pressure caused by centripetal acceleration. There will be a recirculation zone on the lee side of the obstruction.

MODEL FOR HIGH-VELOCITY PRESSURE LOSS IN A SELF-AFFINE ROUGH FRACTURE

We model the inertial resistance as a pressure drag generated by centripetal acceleration of curved flow paths when flow tubes impinges on and bends around fracture roughness. Consider a fluid particle with a local velocity in the angular θ-direction n_q moving in a curve with curvature radius r. The inertial centripetal acceleration results in a pressure gradient in the radial direction ¶p/¶r given by

$$\frac{\partial p}{\partial r} = \frac{r n_q^2}{r} . \tag{6}$$

Note that solid body rotation results in a non-dissipative pressure difference normal to the flow direction.

The pressure gradient in the Forchheimer equation is averaged over the fluid volume, while the velocity is the microscopic velocity averaged over the total volume. To avoid this mismatch in averages, we write a Forchheimer equation based on the interstitial velocity $\tilde{V}$ that is the velocity averaged over the pore volume

$$\tilde{V} = \frac{V}{f} . \tag{7}$$

Based on interstitial velocity the Forchheimer equation (5) can be written

$$-\frac{dp}{dx} = \frac{m}{\tilde{k}_{fh}} \tilde{V} + \tilde{b}\, r\, \tilde{V}^2 , \tag{8}$$

where the interstitial permeability k_{fh} and the interstitial inertial resistance $\tilde{b}$ are given by

$$\tilde{k}_{fh} = \frac{k_{fh}}{f} , \tag{9}$$

and

$$\tilde{b} = f^2 b . \tag{10}$$

The interstitial version of the Forchheimer equation is useful both for modeling inertial resistance and for analyzing high-velocity flow through a single fracture for which the porosity is not a relevant parameter.

A fracture can be modeled as two identical impermeable self-affine surfaces spaced by a fixed width normal to the average fracture plane. Consider a self-affine two-dimensional fracture (channel) of length L. The fracture has two identical self-affine fracture profiles spaced by a fixed width w normal to the average profile line. By self-affinity the root mean square roughness width z over a distance x is a power law

$$z = Ax^{\zeta} . \tag{11}$$

The scale independent amplitude A is in [length$^{1-\zeta}$].

Now we construct a simple model for the inertial resistance based on flow tube impingements. Since impingements are discrete, we model the inertial pressure loss Dp as the number of impingements N times the average pressure loss of one (single) impingement $(Dp)_s$

$$\Delta p = N(\Delta p)_s . \tag{12}$$

A flow tube impinges on the fracture wall when the flow is obstructed. On average, the flow is obstructed when the local roughness width is of a size comparable to the vertical width *w*. Thus, the mean impingement free path (inter impingement distance) of the flow is, by (11), a distance x_0 given by

$$x_0 = \left(\frac{w}{A}\right)^{1/z} . \tag{13}$$

Over the length of the fracture, the average number of impingements is *N*,

$$N = \frac{L}{x_0} . \tag{14}$$

The centripetal pressure gradient is from (6) proportional to the curvature k (the inverse of the curvature radius). We assume that the characteristic curvatures of a flow tube (the bends in Figure 1) are proportional to the curvature of a characteristic obstruction. An analytical function *f(x)* has a curvature defined as

$$k = \frac{1}{r} = \frac{\left| d^2 f / dx^2 \right|}{\left[1 + (df/dx)^2\right]^{3/2}} . \tag{15}$$

Self-affine profiles are not differentiable, but characteristic slopes and curvatures can be estimated by using the statistical properties. We assume that the characteristic slope over the length scales of interest x_0 is much smaller than unity, so that the characteristic curvature of the roughness is described by an estimate of the second derivative over a length scale x_0

$$k(x_0) \approx \left| \frac{\Delta^2 z}{\Delta x^2} \right|_{x_0} \approx O\left(\frac{w}{x_0^2}\right), \tag{16}$$

where the subscript x_0 stresses that the characteristic second differential ("second derivative") is measured over a distance x_0. By combining (6) and $k = 1/r$ the estimated centripetal acceleration pressure difference across the fracture (over a distance *w*) is

$$\frac{\partial p}{\partial r} w = w k \; r \tilde{V}^2 , \tag{17}$$

The characteristic pressure loss associated with one impingement (causing a pressure drag) is proportional to the centripetal acceleration pressure difference (17), so that by using (16) we obtain

$$(\Delta p)_s = C \, w \frac{w}{x_0^2} \, r \tilde{V}^2 , \tag{18}$$

where the constant *C* is of O*(1)*. Subsequent combination of (12), (14), (18), and (13) yields

$$\frac{\Delta p}{L} = C \frac{w^2}{x_0^3} \, r \tilde{V}^2 = C A^{3/z} w^{2-3/z} \, r \tilde{V}^2 , \tag{19}$$

By comparing this pressure loss with the non-linear term in the Forchheimer equation (8) we find that the interstitial inertial resistance is given by

$$\tilde{b} = C A^{3/z} w^{-a} , \tag{20}$$

where the characteristic exponent a is given by

$$a = \frac{3}{z} - 2 . \tag{21}$$

This is our main theoretical result.

Now, can this model be extended to three-dimensional self-affine rough fractures with the same roughness exponent measured in all lateral (fracture plane) directions? We assume that the picture of flow tubes and impingements is valid for the three dimensional situation. In three dimensions the flow may avoid the most extreme obstructions by simply flowing around them in the lateral plane. However, self-affine roughness cannot be avoided. Since the fracture surface is self-affine in any lateral direction, the roughness width *z* experienced on any smooth enough trajectory in the average fracture plane obeys a self-affine

scaling where x is replaced by the length of the trajectory. Thus the pressure loss along a flow tube should also be described by the power law expression of (20) and (21).

EXPERIMENTAL WORK

Cylindrical cores of length 7.45 cm and diameter 3.0 cm were drilled from a block of Berea sandstone with porosity of 0.2, permeability of 450 mD, and average grain size of 203 micrometer. The cores were fractured longitudinally. A core was placed on a wedge and loaded from above by a piston until it fractured. Fragmented samples were discarded. To make fracture and core end surfaces impermeable, they were exposed to fluid epoxy. The epoxy imbibed spontaneously into the core by capillary pressure. Residue was removed from the surfaces by a thin paper cloth. Microscope inspection confirmed that the surface geometry was intact. Each core half was attached to a half cylinder of steel (a shell). The outer diameter was 3.707 cm, the thickness was 3.5 mm (inner diameter was 3.007 cm) and the length was 7.7 cm. The shells were cleaned with acetone, dried, glued to the sandstone core halves with silicon, and pressed together.

Now, consider a fracture formed by two identical self-affine surfaces spaced by a distance w normal to the average fracture plane. Let the average fracture plane be the xy-plane, such that x denotes the longitudinal direction (the flow direction) of total length L, and y the transversal direction of total height h. Let z be in the direction of the unit normal of the average fracture plane, so that w is along z. The cross-sectional area of the fracture S_f is given by

$$S_f = wh . \tag{22}$$

The average fracture plane has an area Lh.

When the steel shells are pressed together, the fracture closes imperfectly, so that there will be a residual fracture space. At best this is the sandstone pore space. The residual fracture space was modeled as a residual fracture width w_0. An apparent fracture width w_a was controlled by the thickness of two equally sized steel shims (spacers) inserted between the edges of the shells. They were 3.5 mm wide and 7.7 cm long. The thickness of the shims varied from 50 micrometer to 1 mm in steps of 50 micrometer. The total average fracture width w is the sum of the apparent and residual fracture widths

$$w = w_a + w_0 . \tag{23}$$

We guess that the size of w_0 is of the order of the size of one average Berea sand grain.

The measurements of fracture roughness $z(x,y)$ are briefly described in (Skjetne *et al.* 1998). The roughness was measured by profilometry and analyzed by two methods: Fourier power spectrum and average wavelet coefficients. Both methods confirmed that the fracture surfaces were self-affine with $\zeta = 0.75$ from averaged Fourier power spectra and ζ = 0.67 from averaged wavelet coefficients (AWC method). The self-affine lower cutoff was close to the average grain size. Below the cutoff, the surface geometry was controlled by the shape of the grains. The amplitude on the core scale was about 3 mm.

The flow setup is shown in Figure 2. The fluid was 99.5% by weight pure nitrogen. The fractured samples were held in place by a water controlled piston and an enclosing sleeve in the core holder. Differential pressure over the fracture length, flow rate, atmospheric pressure and temperature were measured. Pressure differences were measured between the sample end faces in the range from 0.001 to 3 bar. The mass rate was measured upstream of the fractured core sample in the range from 0.001 to 50 Sl/min. Standard liter (Sl) refers to T = 0 ^{o}C and p = 1.013 bar. A pressure gauge was mounted at the entrance of the core holder. The gas was led through a 6 m by ¼ in. outer diameter copper coil through a temperature regulated water bath (heat exchanger) to counteract the Joul-Thompson effect.

The data were analyzed by the Forchheimer equation integrated over the length L of the core

$$\frac{\left(p_1^{\,2} - p_2^{\,2}\right)M}{2ZRTL} = \frac{m}{k_{fh}}\, rV + b\left(rV\right)^2 , \tag{24}$$

where p_1 and p_2 are the upstream and downstream pressures, M is the molecular weight of nitrogen, Z is the gas compressibility, and R is the universal gas constant.

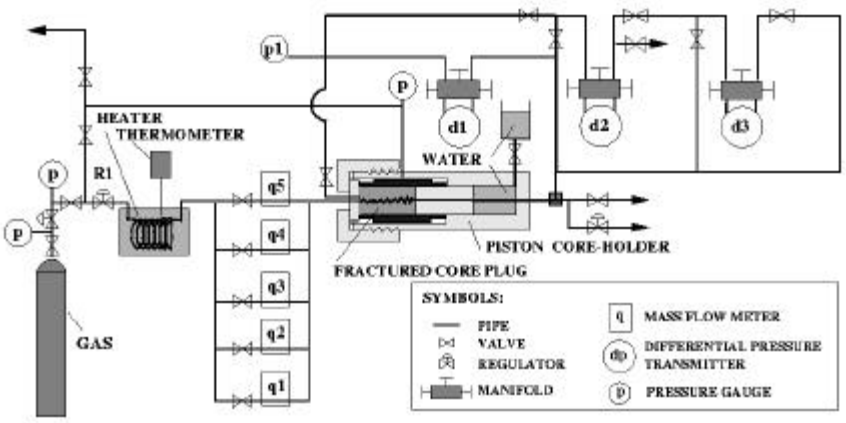

Figure 2. Flow setup.

A Darcy plot is a plot of the left-hand side of (24) versus the mass flux rV. To obtain (24) we have first multiplied both sides of the Forchheimer equation (5) by the density. Next, we used the gas law

$$r = \frac{M}{ZRT}\, p\,, \tag{25}$$

for the density on the left-hand side. For the integration we used that steady flow and mass balance demand that the mass flux is constant and assumed that T, m, and Z are constants, which is a reasonable assumption for small pressure differences. In our experiments the pressure difference was less than three bar. We ignored finite size effects and also any effects of Klinkenberg wall slip flow (Skjetne and Auriault, 1999c). To obtain rV, we divide the mass rate by an area S, which can be chosen arbitrary. We chose

$$S = \frac{p\, h^2}{4} \quad \left(= 7.07\times 10^{-4}\,\mathrm{m}^2\right), \tag{26}$$

which is equal to the cross-sectional area of a core with a diameter of 30 mm. In this formulation

$$f = \frac{S_f}{S} = \frac{wh}{S} = \frac{\left(w_a + w_0\right)h}{S}\,. \tag{27}$$

A Forchheimer plot is a plot of the left hand side of (24) divided by the mass flux versus the mass flux,

$$\frac{\left(p_1{}^2 - p_2{}^2\right)M}{2ZRTL\, rV} = \frac{m}{k_{fh}} + b\, rV\,. \tag{28}$$

Data following the Forchheimer equation are on a straight line with a slope equal to b and an extrapolated zero crossing equal to m/k_{fh} where m = 1.74×10^{-5} Pa·s. We fitted (28) to the flow data to determine b and k_{fh}. However, we present Forchheimer plots where the mass flux is replaced by an interstitial Reynolds number, which is obtained by replacing v and l in (1) by $\tilde{V}$ and w

$$Re = \frac{r\, w\tilde{V}}{m} \quad \left(= \frac{\left(r\,V\right)S}{m\,h}\right). \tag{29}$$

Combination of (28) and (29) yields

$$\frac{\left(p_1{}^2 - p_2{}^2\right)M}{2ZRTL\, rV} = \frac{m}{k_{fh}} + b\,\frac{m\,h}{S}\,Re\,. \tag{30}$$

A relationship between $\tilde{b}$ and b is derived by combining (10), (26) and (27)

$$\tilde{b} = j^2 b = \frac{h^2 w^2}{S^2} b = \frac{16 w^2}{p^2 h^2} b \ . \qquad (31)$$

To write the model (20) and (21) in terms of *b(w)* we use (31)

$$\frac{16b}{p^2 h^2} = C_1 w^{-(a+2)} = C_1 \left(w_a + w_0\right)^{-(a+2)} = C_1 \left(w_a + w_0\right)^{-3/z} , \qquad (32)$$

where

$$C_1 = CA^{3/z} \ . \qquad (33)$$

The unknown parameters in the model are C_1, w_0, and a (or z). The model (32) was least squares fitted to the data (essentially b and w_a) by first taking the logarithm of base 10 on each side of (32)

$$\log\left(\frac{16b}{p^2 h^2}\right) = \log(C_1) - (a+2)\log\left(w_a + w_0\right), \qquad (34)$$

The results of the fit are: C_1, w_0, and a. Knowing w_0, we calculated $\tilde{b}$ by (31) and w by (23).

RESULTS AND DISCUSSION

Results of high-velocity flow experiments performed on 20 fractures are shown in Table 1. The parameter k_{sf} (= $w^2/12$) is the permeability for flow between flat plates. The flow rates varied from 3.67×10^{-6} to 8.33×10^{-4} m^3/s. This gives $Re \in$ [8, 1861]. The minimum Reynolds number increased with fracture width because the pressure loss decreased with fracture width and fell below the pressure transmitter lower range limit. Transition from laminar to turbulent flow in a flat fracture is at about Re = 1400 and in a rough fracture at a lower Reynolds number. We expect that the flow is turbulent for the highest velocity data.

w_a [μm]	w [μm]	k_{fh} [m^2]	$\tilde{k}_{fh}$ [m^2]	k_{sf} [m^2]	b [1/m]	$\tilde{b}$ [1/m]
50	250	2.68×10^{-11}	2.53×10^{-9}	5.21×10^{-9}	9.61×10^{6}	1.09×10^{3}
100	300	4.64×10^{-11}	3.64×10^{-9}	7.50×10^{-9}	5.23×10^{6}	8.50×10^{2}
150	350	8.54×10^{-11}	5.74×10^{-9}	1.02×10^{-8}	2.60×10^{6}	5.76×10^{2}
200	400	1.63×10^{-10}	9.57×10^{-9}	1.33×10^{-8}	1.68×10^{6}	4.86×10^{2}
250	450	2.61×10^{-10}	1.37×10^{-8}	1.69×10^{-8}	1.02×10^{6}	3.73×10^{2}
300	500	5.57×10^{-10}	2.62×10^{-8}	2.08×10^{-8}	6.63×10^{5}	2.99×10^{2}
350	550	1.04×10^{-9}	4.44×10^{-8}	2.52×10^{-8}	4.63×10^{5}	2.53×10^{2}
400	600	2.22×10^{-9}	8.72×10^{-8}	3.00×10^{-8}	3.38×10^{5}	2.20×10^{2}
450	650	3.07×10^{-9}	1.11×10^{-7}	3.52×10^{-8}	2.46×10^{5}	1.88×10^{2}
500	700	2.56×10^{-9}	8.62×10^{-8}	4.08×10^{-8}	1.97×10^{5}	1.74×10^{2}
550	750	9.75×10^{-9}	3.06×10^{-7}	4.69×10^{-8}	1.28×10^{5}	1.30×10^{2}
600	800	7.42×10^{-9}	2.18×10^{-7}	5.33×10^{-8}	1.04×10^{5}	1.20×10^{2}
650	850	-7.30×10^{-8}	-2.02×10^{-3}	6.02×10^{-8}	8.28×10^{4}	1.08×10^{2}
700	900	-3.94×10^{-8}	-1.03×10^{-3}	6.75×10^{-8}	7.15×10^{4}	1.04×10^{2}
750	950	1.07×10^{-8}	2.64×10^{-7}	7.52×10^{-8}	5.91×10^{4}	9.61×10^{1}
800	1000	-4.08×10^{-8}	-9.61×10^{-7}	8.33×10^{-8}	4.31×10^{4}	7.78×10^{1}
850	1050	9.97×10^{-9}	2.24×10^{-7}	9.19×10^{-8}	4.10×10^{4}	8.15×10^{1}
900	1100	-1.36×10^{-8}	-2.90×10^{-7}	1.01×10^{-7}	3.05×10^{4}	6.66×10^{1}
950	1150	1.73×10^{-8}	3.54×10^{-7}	1.10×10^{-7}	2.93×10^{4}	6.99×10^{1}
1000	1200	-1.76×10^{-8}	-3.46×10^{-7}	1.20×10^{-7}	2.13×10^{4}	5.53×10^{1}

Table 1. Experimental results and fracture data (w_0 = 200 micrometer).

Three pairs of Darcy and Forchheimer plots are shown in Figures 3 – 8, with apparent fracture widths of 50, 500 and 950 micrometer. The Darcy plot flow data are given in Appendix A.

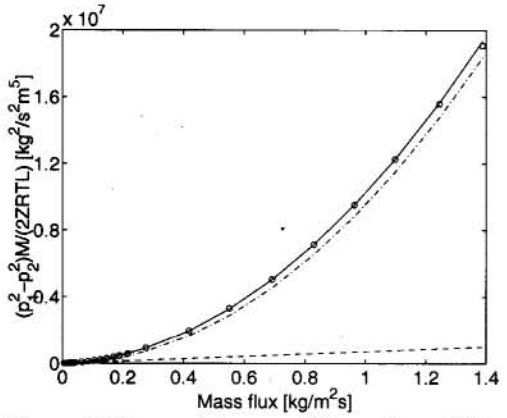

Figure 3. Darcy plot. w_a = 50 μm (w = 250 μm). (Circles) experimental data, (solid line) Equation (24), (dashed line) linear term of (24) and (dashdot line) square term of (24).

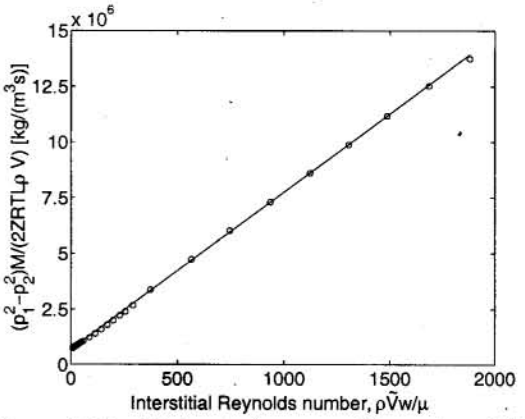

Figure 4. Forchheimer plot. w_a = 50 μm (w = 250 μm). (Circles) experimental data and (solid line) Equation (30).

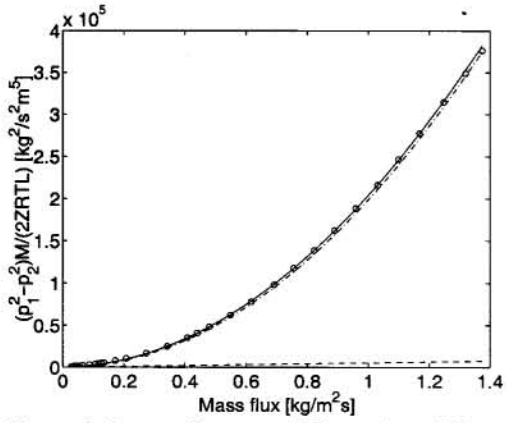

Figure 5. Darcy plot. w_a = 500 μm (w = 700 μm).

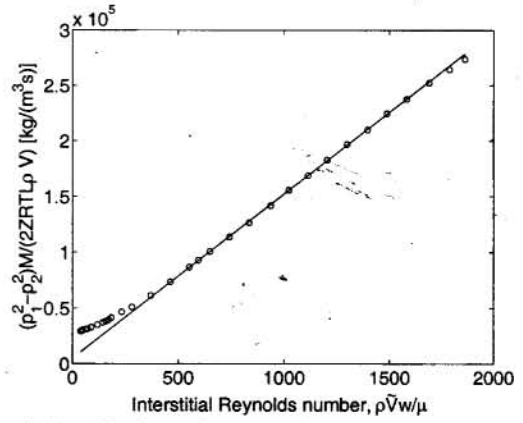

Figure 6. Forchheimer plot. w_a = 500 μm (w = 700 μm).

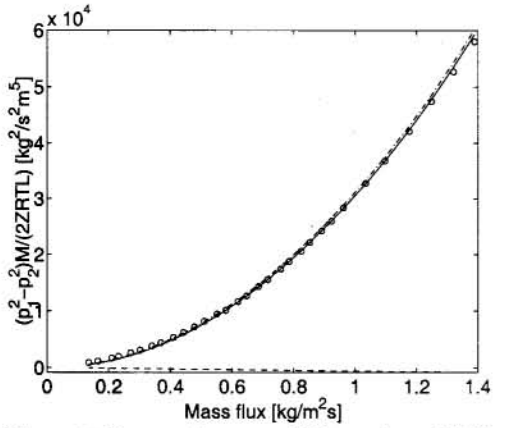

Figure 7. Darcy plot. w_a = 950 μm (w = 1150 μm).

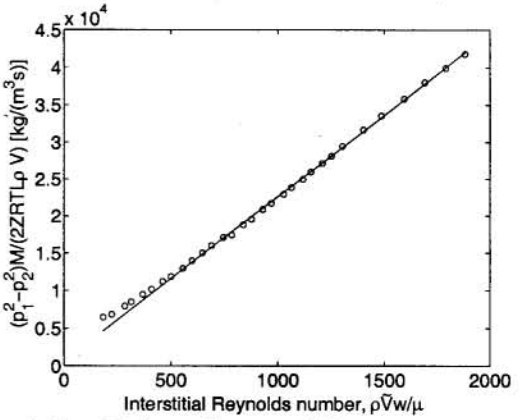

Figure 8. Forchheimer plot. w_a = 950 μm (w = 1150 μm).

The Darcy plots show the contributions from the Darcy (dashed line) and Forchheimer (dashdot line) terms in the Forchheimer equation (24) (solid line). For large mass fluxes the Forchheimer term dominates over the Darcy term. The Darcy term decreases systematically for increasing fracture widths and turns even negative. This means that the Forchheimer permeability is negative for some of the larger fracture widths.

The Forchheimer plots in Figures 4, 6, and 8, show that (30) does not fit the data for the lowest Reynolds numbers. The data curve up with increasing rate. This is typical for a weak inertia flow regime. The Reynolds number, for the crossover from the weak inertia to the Forchheimer regime, increases with increasing fracture width. The Forchheimer plot of small width fractures such as shown in Figure 4 (w = 250 micrometer) display no clear indication of a weak inertia regime. The crossover in Figure 6 (w = 700 micrometer) and 8 (w = 1150 micrometer) are approximately at Re = 400 and Re = 800.

The Forchheimer equation is fitted to the data in the Forchheimer regime. The match is quite good, except for the highest Reynolds number data. No clear indication of a transition to turbulence can be seen in the data. However, a transition to turbulence is not well defined for rough fractures, and we do not know exactly how a transition should be reflected in the resistance data.

We fitted the parameters C_1, w_0, and a in (34) to the b versus w_a from (28). In Figure 9 we present the result in terms of $\tilde{b}$ -factors, calculated by (31), versus total fracture width w in log-log coordinates together with the fit of the model (34). We estimated the 95% confidence interval for the parameters by using the fit and the flow data at the solution. The fit results are presented in Table 2.

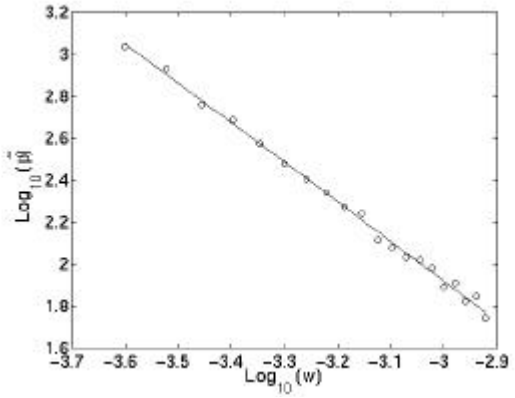

Figure 9. (Circles) $\tilde{b}$ -factor versus fracture width and (solid line) fit.

Parameter	Value	95% Confidence Interval
C_1 [m^{a-1}]	185×10^{-6}	$[32.26\times 10^{-6}, 1.06\times 10^{-3}]$
a	1.88	[1.62, 2.15]
z	0.77	[0.72, 0.83]
w_0 [μm]	200	[164, 237]

Table 2. Fit results.

The size of w_0 was 200 micrometer, which is close to the average size of a Berea sand grain. This seems to be a reasonable size for w_0. However, we cannot exclude that w_0 has no obvious physical meaning. By fixing w_0 = 0 micrometer, the model (34) does not fit the data well. However, in the following we treat w with w_0 = 200 micrometer as the true fracture width.

Our main experimental result is the correlation (Figure 9)

$$\tilde{b} = 185\times10^{-6}\, w^{-1.88}, \qquad (35)$$

where w is in [meter] and $\tilde{b}$ is in [1/meter]. By using (20) and (21), the power in (35) corresponds to

$$z = 0.77. \qquad (36)$$

Interestingly, the roughness exponent (36) from flow experiments is close to the roughness exponent from the profilometry measurements.

CONCLUSIONS

- High-velocity pressure loss in a self-affine rough channel of fixed width was modeled to be square in velocity, and a power law in fracture width, where the power is given by the self-affine roughness exponent. The pressure loss was caused by a pressure drag generated by centripetal acceleration. The model may be applicable to three-dimensional self-affine fractures.
- High-velocity pressure loss in self-affine fractures in Berea sandstone, was described by a Forchheimer equation with a dominating square term in velocity. The square term was a power law in fracture width. The power agreed well with the power predicted from the model.
- For some larger fracture widths the Forchheimer linear term (permeability) was negative.
- A weak inertia flow regime separated the Darcy and Forchheimer flow regimes.

ACKNOWLEDGEMENTS

T. Kløv thanks the Nordic Energy Research Programme, Statoil and Norsk Hydro for their financial support through the project "High-Velocity Flow in Fractures". T. Kløv also thanks the Norwegian Formation Evaluation Society (NFES) for their financial support related to the presentation of this paper.

NOMENCLATURE

A = Self-affine amplitude, $L^{1-\zeta}$, $m^{1-\zeta}$
C = Constant
L = Fracture length in flow direction, L, m
M = Molecular weight, m, g/mol
N = Number of impingements
R = Universal gas constant, 8.314 J/(molK)
Re = Reynolds number
S = Surface area, L^2, m^2
T = Temperature, K
V = Seepage velocity, L/T, m/s
Z = Gas compressibility factor
a = Permeability exponent
b = Correlation constant, L^{2a-1}, m^{2a-1}
c = Porosity exponent
f = Function
h = Fracture height = core diameter, L, m
k = Permeability, L^2, m^2 or mD
l = Typical microscopic length scale, L, m
p = Pressure, $m/(T^2L)$, Pa or bar
r = Radial coordinate, L, m
v = Typical microscopic velocity, L/T, m/s
w = Fracture width, L, m
x = Cartesian coordinate, L, m
y = Cartesian coordinate, L, m
z = Cartesian coord., roughness width, L, m

Greek letters

α = Inertial resistance model power exponent
β = Inertial resistance coefficient, 1/L, 1/m
ϕ = Porosity
γ = Weak inertia coefficient
κ = Curvature
μ = Fluid viscosity, m/(TL), Pa·s
ρ = Fluid density, m/L^3, kg/m^3
ζ = Self-affine roughness exponent

Subscripts

0 = Impingement free (path), residual (width)
a = Apparent
fh = Forchheimer
s = Single impingement
sf = Smooth parallel plate fracture
θ = Angular

Embellishment

$\sim$ = Interstitial (averaged over pore space)

REFERENCES

Barrére, J., "Modelisation des ecoulements de Stokes et Navier-Stokes en milieu poreux", Doctoral thesis at Universite de Bordeaux I, (1990).

Bertuzzi F., Sanfilippo F. and Brignoli M., "Characterization of flow within natural fractures: numerical simulations and field applications", Proceednings from the SPE/IRMS Eurock'98 Conference in Trondheim, (1998), 337-345.

Brown S. R., "Fluid flow through rock joints: the effect of surface roughness", *J. Geophys. Res.*, (1987) **92**, B2, 1337-1347.

Boffa, J. M., Allain, C. and Hulin, J. P., "Experimental analysis of fracture rugosity in granular and compact rocks", *Eur. Phys. J. AP*, (1998) **2**, 281-289.

Du Plessis, J. P., "Analytical Quantification of coefficients in the Ergun equation for fluid friction in a packed bed", *Transport in Porous Media*, (1994) **16**, 189 – 207.

Firdadouss, M. and Guermond, J., "Sur l'homogénéisation des équations de Navier-Stokes à faible nombre de Reynolds", C. R. Acad. Sci. Paris, Série I, (1995) **320**, 245-251.

Firoozabadi, A. and Katz, D.L., "An analysis of high-velocity gas flow through porous media", *J. Petrol. Tech*., (1979) **Feb**, 211-216.

Forchheimer, P., "Wasserbewegung durch Boden", *Zeitschrift des Vereines deutcher Ingenieure*, (1901) **45**, 50, 1781-1788.

Fourar, M. and Lenormand, R., "A viscous coupling model for relative permeabilities in fractures", Proceedings from the 1998 International Symposium of the Society of Core Analysts in The Hague, The Netherlands, (1998), SCA-9825.

Gutfraind R. and Hansen A., "Study of fracture permeability using lattice gas automata", *Transport in Porous Media*, (1995) **18**, 131-149.

Jones, T. A., Wooten, S. O., and Kaluza, T. J., "Single phase flow through natural fractures", paper SPE 18175, (1988), 687 – 696.

Mahoney, D., and Doggett, K., "Multiphase flow in fractures", Proceedings from the 1997 International Symposium of the Society of Core Analysts in Calgary, Canada, (1997).

Mei, C. C. and Auriault, J.-L., "The effect of weak inertia on flow through a porous medium", *J. Fluid Mech*., (1991), **222**, 647-663.

Noman, R. and Archer, J. S., "The effect of pore structure on non-Darcy gas flow in some low-permeability reservoir rocks", paper SPE/DOE 16400, (1987).

Rasoloarijaona M. and Auriault, J.-L., "Nonlinear seepage flow through a rigid porous medium", *Eur. J. Mech. B/Fluids*, (1994) **13**, 177-195.

Schmittbuhl, J., Schmitt, F., and Scholz, C., "Scaling invariance of crack surfaces", *J. Geophys. Res.*, (1995) **100**, B4, 5953-5973.

Schrauf, T. W. and Evans, D. D. "Laboratory studies of gas flow through a single natural fracture", Water Resources Res., (1986) **22**, 7, 1028 – 1050.

Skjetne, E., and Auriault, J.-L., "New insights on steady, non-linear flow in porous media", *Eur. J. Mech. B/Fluids*, (1999a) **18**, 1, 131-145.

Skjetne, E., and Auriault, J.-L., "High-velocity laminar and turbulent flow in porous media", Accepted for publication in *Transport in Porous Media*, (1999b).

Skjetne, E., and Auriault, J.-L., "Homogenization of wall-slip gas flow through porous media", Accepted for publication in *Transport in Porous Media*, (1999c).

Skjetne, E., Hansen, A., and Gudmundsson, J. S., "High-velocity flow in a rough fracture", *J. Fluid Mech.*, (1999) **383**, 1-28.

Skjetne, E., Kløv, T., and Gudmundsson, J. S., "Innovation in fracture roughness characterization", Proceedings from the 1998 International Symposium of the Society of Core Analysts in The Hague, The Netherlands, (1998), SCA-9844.

Wodie, J.-C. and Levy, T.,"Correction non linéaire de la loi de Darcy", C. R. Acad. Sci. Paris, Série II, (1991) **312**, 157-161.

Zimmerman R. W., Bodavarsson G. S., "Hydraulic conductivity of rock fractures", *Transport in Porous Media*, (1996) **23**, 1-30.

APPENDIX A: FLOW DATA FOR DARCY PLOTS

Figure 3 w_a **= 50 μm**	***Figure 3*** w_a **= 50 μm**	***Figure 5*** w_a **= 500 μm**	***Figure 5*** w_a **= 500 μm**	***Figure 7*** w_a **= 950 μm**	***Figure 7*** w_a **= 950 μm**
Mass Flux rV [kg/m^{2}s]	Pressure Loss $\frac{(p_1^2 - p_2^2)M}{2ZRTL}$ [kg^2/s^{2}m^5]	Mass Flux rV [kg/m^{2}s]	Pressure Loss $\frac{(p_1^2 - p_2^2)M}{2ZRTL}$ [kg^2/s^{2}m^5]	Mass Flux rV [kg/m^{2}s]	Pressure Loss $\frac{(p_1^2 - p_2^2)M}{2ZRTL}$ [kg^2/s^{2}m^5]
1.3884	1.9082×10^{7}	1.3746	3.7621×10^{5}	1.3899	5.8074×10^{4}
1.2448	1.5582×10^{7}	1.3201	3.4896×10^{5}	1.3216	5.2711×10^{4}
1.0978	1.2260×10^{7}	1.2478	3.1474×10^{5}	1.2492	4.7469×10^{4}
9.6325×10^{-1}	9.5116×10^{6}	1.1685	2.7742×10^{5}	1.1770	4.2140×10^{4}
8.2921×10^{-1}	7.1370×10^{6}	1.0992	2.4660×10^{5}	1.0978	3.6826×10^{4}
6.9157×10^{-1}	5.0509×10^{6}	1.0309	2.1622×10^{5}	1.0350	3.2775×10^{4}
5.5081×10^{-1}	3.3178×10^{6}	9.5912×10^{-1}	1.8855×10^{5}	9.6187×10^{-1}	2.8319×10^{4}
4.1765×10^{-1}	1.9757×10^{6}	8.8926×10^{-1}	1.6238×10^{5}	9.2346×10^{-1}	2.5940×10^{4}
2.7604×10^{-1}	9.3170×10^{5}	8.2240×10^{-1}	1.3878×10^{5}	8.9199×10^{-1}	2.4184×10^{4}
2.1566×10^{-1}	5.7680×10^{5}	7.5563×10^{-1}	1.1767×10^{5}	8.5240×10^{-1}	2.2121×10^{4}
1.8876×10^{-1}	4.5313×10^{5}	6.9157×10^{-1}	9.7997×10^{4}	8.2512×10^{-1}	2.0575×10^{4}
1.6951×10^{-1}	3.7677×10^{5}	6.1649×10^{-1}	7.7986×10^{4}	7.8560×10^{-1}	1.8722×10^{4}
1.4688×10^{-1}	2.9446×10^{5}	5.4807×10^{-1}	6.2261×10^{4}	7.5836×10^{-1}	1.7385×10^{4}
1.2619×10^{-1}	2.2776×10^{5}	4.7948×10^{-1}	4.8268×10^{4}	7.1611×10^{-1}	1.5535×10^{4}
1.0540×10^{-1}	1.6873×10^{5}	4.3964×10^{-1}	4.0836×10^{4}	6.8612×10^{-1}	1.4303×10^{4}
8.4514×10^{-2}	1.1904×10^{5}	4.0802×10^{-1}	3.5335×10^{4}	6.4791×10^{-1}	1.2662×10^{4}
6.3965×10^{-2}	7.8094×10^{4}	3.4200×10^{-1}	2.5120×10^{4}	6.1922×10^{-1}	1.1638×10^{4}
4.2519×10^{-2}	4.4019×10^{4}	2.7329×10^{-1}	1.6740×10^{4}	5.7956×10^{-1}	1.0102×10^{4}
3.5439×10^{-2}	3.5475×10^{4}	2.0752×10^{-1}	1.0586×10^{4}	5.5081×10^{-1}	9.4204×10^{3}
3.2447×10^{-2}	3.1530×10^{4}	1.7203×10^{-1}	8.0130×10^{3}	5.0968×10^{-1}	8.1580×10^{3}
2.9446×10^{-2}	2.8008×10^{4}	1.3533×10^{-1}	5.6108×10^{3}	4.7811×10^{-1}	7.1839×10^{3}
2.6826×10^{-2}	2.4804×10^{4}	1.3572×10^{-1}	5.5865×10^{3}	4.4239×10^{-1}	6.1785×10^{3}
2.3725×10^{-2}	2.0987×10^{4}	1.2661×10^{-1}	5.0027×10^{3}	4.1077×10^{-1}	5.3172×10^{3}
2.1117×10^{-2}	1.8310×10^{4}	1.1664×10^{-1}	4.4596×10^{3}	3.6951×10^{-1}	4.3766×10^{3}
1.8077×10^{-2}	1.5330×10^{4}	1.0623×10^{-1}	3.9491×10^{3}	3.4063×10^{-1}	3.8190×10^{3}
1.5068×10^{-2}	1.2252×10^{4}	8.7443×10^{-2}	3.0662×10^{3}	3.0213×10^{-1}	3.0704×10^{3}
1.1918×10^{-2}	9.4876×10^{3}	6.5225×10^{-2}	2.1352×10^{3}	2.7192×10^{-1}	2.5768×10^{3}
1.1679×10^{-2}	9.2766×10^{3}	5.3037×10^{-2}	1.6659×10^{3}	2.3215×10^{-1}	1.9720×10^{3}
9.1711×10^{-3}	7.0881×10^{3}	4.5044×10^{-2}	1.3908×10^{3}	2.1026×10^{-1}	1.6697×10^{3}
5.9417×10^{-3}	4.3766×10^{3}	3.5721×10^{-2}	1.0915×10^{3}	1.6522×10^{-1}	1.1288×10^{3}
—	—	3.3238×10^{-2}	9.8640×10^{2}	1.3533×10^{-1}	8.7438×10^{2}
—	—	2.8423×10^{-2}	8.3274×10^{2}	—	—

Table A1. Flow data for the Darcy plots of Figures 3, 5, and 7. Forchheimer plot (Figures 4, 6, and 8) data are obtained by dividing the each "Pressure Loss" in this table by the respective "Mass Flux". The table is ordered in the sequence the experiments were performed (1st row is 1st measurement).